Available online at www.sciencedirect.com
SCIENCE DIRECT®
Remote Sensing of Environment 102 (2006) 344–363
Remote Sensing of Environment
www.elsevier.com/locate/rse

Retrieval of mineral aerosol optical depth and size information from Meteosat Second Generation SEVIRI solar reflectance bands

H.E. Brindley [a,*], A. Ignatov [b]

[a] Space and Atmospheric Physics Group, Imperial College, London, UK
[b] NOAA/NESDIS/Office of Research and Applications, Camp Springs, Maryland, USA

Received 11 July 2005; received in revised form 30 November 2005; accepted 27 February 2006

Abstract

The current operational algorithm used to retrieve aerosol optical depth and Ångström exponent over ocean from the solar reflectance bands of the Advanced Very High Resolution Radiometer (AVHRR) flown onboard NOAA polar orbiting satellites was adapted to the corresponding channels of the Spinning Enhanced Visible and Infra-Red Imager (SEVIRI) flown onboard the Meteosat Second Generation (MSG) geostationary platform. By examining two specific dust events from 3–5 March and 12–13 October 2004 we show how a detailed description of the dust loading through the diurnal cycle can be obtained. Snapshot comparisons with spatially resolved retrievals from the MODerate resolution Imaging Spectrometer (MODIS) instruments flown on the *Terra* and *Aqua* polar platforms show qualitative agreement with SEVIRI retrievals. In addition to the generic aerosol model used in the NOAA/NESDIS algorithm, which was tuned to optimize retrievals over global ocean, three microphysical models, specifically proposed in the aerosol literature for desert dust, have also been tested. However, comparison of the diurnal variation seen in these SEVIRI retrievals with available ground based Aerosol Robotic Network (AERONET) observations from two coastal stations suggests that the phase functions associated with two of these dust representations, obtained under the assumption of particle sphericity, result in unrealistic time dependent behaviour. This tendency is removed when either the generic aerosol representation used in the NOAA/NESDIS algorithm is employed, or a more physically based non-spherical dust representation is used.
© 2006 Elsevier Inc. All rights reserved.

Keywords: Dust aerosol; Geostationary satellite observations; Diurnal cycle; Microphysical aerosol models

1. Introduction

Brindley & Russel (2006, submitted for publication), described a methodology to detect mineral dust events using information from the thermal infrared channels on the Spinning Enhanced Visible and Infrared Imager (SEVIRI) flying on Meteosat Second Generation (MSG; renamed after launch to Meteosat-8, Schmetz et al., 2002). This detection is necessary to improve the scene identification used within the routine processing of observations from the Geostationary Earth Radiation Budget (GERB) instrument, (Harries et al., 2005), mounted on the same satellite. This technique also permitted a crude estimate of mineral aerosol optical depth (AOD). However, during sunlit hours, and outside of regions of sun-glint a more conventional method using the three SEVIRI solar reflectance channels at 0.6, 0.8 and 1.6 μm can be employed. The use of multiple channel information should also provide an estimate of the aerosol size. These channels are sensitive to not only mineral dust but to all the major aerosol types such as those arising from biomass burning, the main anthropogenic aerosol species in the region considered here. However, this potential is not directly explored in this study which concentrates on the dust analyses. Furthermore, the potential for the presence of biomass aerosols to influence the retrievals presented here is small because burning activity is most intense over north Africa from December–February, outside of the time periods investigated here.

This study takes advantage of the existing National Oceanic Atmospheric Administration/National Environmental Satellite, Data and Information Service (NOAA/NESDIS) third generation aerosol retrieval algorithm developed for the Advanced Very High Resolution Radiometer (AVHRR) onboard NOAA polar orbiting satellites (Ignatov & Stowe, 2002) and adapts it to the SEVIRI instrument characteristics. The close proximity of

* Corresponding author. Tel.: +44 207 5947673; fax: +44 207 5947900.
E-mail address: h.brindley@imperial.ac.uk (H.E. Brindley).

0034-4257/$ - see front matter © 2006 Elsevier Inc. All rights reserved.
doi:10.1016/j.rse.2006.02.024

the AVHRR/3 channels (centred at 0.63, 0.83 and 1.61 μm) to their SEVIRI counterparts makes modification of the algorithm to incorporate the different instrument spectral responses relatively straightforward, thus permitting the use of a robust, well validated AVHRR retrieval methodology on the new SEVIRI observations.

Note that an AVHRR-like "A product" has also been generated from the Visible Infra-Red Scanner (VIRS) onboard the highly precessing Tropical Rainfall Measuring Mission (TRMM) platform, and more recently from the two MODIS instruments onboard the *Terra* and *Aqua* polar orbiting satellites. The single-channel secondary A product derived from MODIS radiances is available, in addition to the multi-channel MOD04-based "M product", from the Clouds and Earth's Radiant Energy System (CERES) Single Scanner Footprint (SSF) *Terra* and *Aqua* datasets generated by the CERES Science Team at NASA/LaRC (Ignatov et al., 2005). The single-channel A product on the CERES SSF was shown to compare well with the more comprehensive multi-spectral M product. One benefit of collaboration between the US CERES and European GERB radiation balance project teams is the extension of this approach to the SEVIRI observations, ensuring consistency with the AVHRR, VIRS, and MODIS single-channel aerosol products, and preserving the heritage of the existing aerosol records.

In addition, testing the AVHRR algorithm with SEVIRI observations has the potential to improve the A product. The NESDIS single-channel algorithm was designed and tuned to accurately monitor *globally-average* oceanic aerosol from polar platforms, which take observations under more or less consistent illumination conditions, orbit after orbit. It is thus feasible that the retrievals may be susceptible to systematic aerosol-type specific biases, and perform non-uniformly under a wider range of illumination geometries. The SEVIRI instrument is well placed to capture seasonal and regional variations in aerosol emission from both natural sources (e.g. desert dust outbreaks) and human activities (e.g. biomass burning episodes), allowing detailed testing of the AVHRR-like algorithm under these contrasting aerosol types. Previous studies have shown how long-term climatologies of Saharan dust loading and transport over the North Atlantic and Mediterranean can be derived over specific time-periods using observations from the Meteosat series of instruments (Jankowiak & Tanré, 1991; Moulin et al., 1997). However both of these studies employed information from the one broad visible channel available (spectral width approx. 0.4–1.1 μm, dependent upon satellite) from one time-slot per day (11:30–12:00 UTC). The additional information contained within the three SEVIRI bands can be used to infer aerosol size information. Moreover, by exploiting the full diurnal sampling seen from a geostationary orbit, any angular biases caused by deviation of the aerosol phase function assumed in the retrieval model from the actual aerosol type can be detected and understood. Eventually, these two types of new SEVIRI capabilities should permit improvements to the aerosol and surface models used in the generic NESDIS algorithm to be made.

The aim of this study is thus to perform detailed analyses on two selected case studies, from 3–5 March and 12–13 October 2004, to show how the information available from SEVIRI can be utilized to address these questions. It should be stressed that the findings presented here are limited to these two cases. More complete statistical analyses incorporating many more data and including detailed comparisons with retrievals from the MODIS and AVHRR/3 instruments are planned and will be reported in future publications.

Section 2 provides an overview of the existing AVHRR 3rd generation algorithm, based on the Second Simulation of the Satellite Signal in the Solar Spectrum radiative transfer (RT) model (6S; Vermote et al., 1997a,b). In addition to the generic aerosol model used operationally in the algorithm, the impact of incorporating three different aerosol microphysical models is also tested. The first of these models is taken from the Optical Properties of Aerosols and Clouds (OPAC) database (Hess et al., 1998), and is intended to represent desert dust. The second is the desert model proposed by Shettle (1984) and recommended by the World Meteorological Organization (1983, 1986). Finally, the third model is based on average retrievals of dust size distribution and spectral refractive indices from AERONET observations, which have been used as input to a non-spherical scattering code (Dubovik et al., 2002a,b). As these models have been proposed in the literature specifically to characterise desert dust they may provide better quality retrievals in the presence of

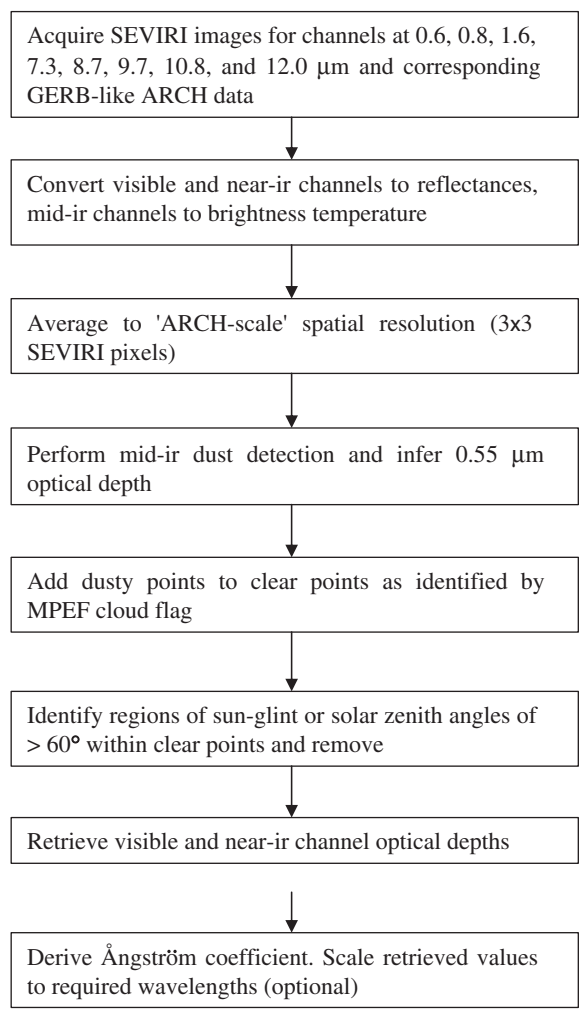

Fig. 1. Schematic showing SEVIRI aerosol retrieval processing chain.

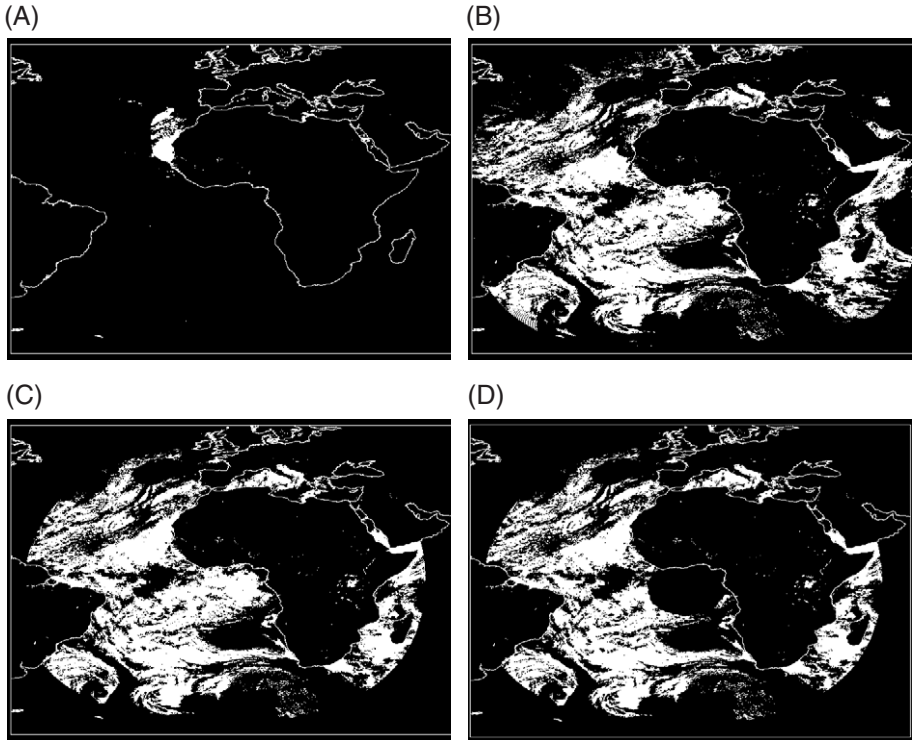

Fig. 2. Derivation of 'clear' points array for application of aerosol retrieval algorithm for 12:00 UTC time-slot on 4th March, 2004. White hatching shows: (A) dusty points identified by infra-red detection algorithm (Brindley, submitted for publication); (B) clear points from MPEF cloud flag (Lutz, 1999); (C) combination of (A) and (B) for solar and view zeniths < 60°, (D) as (C) with sun-glint contaminated points removed.

a dust layer than those obtained with the generic aerosol microphysics used in the NESDIS algorithm.

We then apply the NESDIS and the three additional retrieval algorithms to two dust outbreaks observed by the SEVIRI instrument (Section 3). The spatial pattern of the SEVIRI retrievals is compared to similar quantities derived from observations made by the Moderate Imaging Spectrometer (MODIS) instruments onboard the *Terra* and *Aqua* platforms (Remer et al., 2005; Tanré et al., 1997), while the ability of the retrievals to capture the temporal evolution of both events is diagnosed through comparison with cloud-screened observations from selected Aerosol Robotic Network (AERONET) ground based sites (Holben et al., 1998; Smirnov et al., 2000).

Conclusions and areas for further work are discussed in Section 4.

2. Data processing methodology

This section describes the general data processing which is also summarized in Fig. 1. The subsections below describe the data, explain how pixels suitable for aerosol retrievals are sampled, then give radiometric definitions for the SEVIRI solar reflectance bands, describe aerosol and surface reflectance models, and define output quantities.

2.1. Data

The primary motivation for this work was to obtain an aerosol detection and quantification routine, which could be employed operationally in the GERB data processing chain (Brindley & Russel, 2006, submitted for publication). The 'GERB-like' level 2 ARCH (GL2A) product is employed, which comprises a 15 min snapshot of broad-band radiances derived from SEVIRI data using a narrow to broad-band conversion algorithm developed at the Royal Meteorological Institute of Belgium (RMIB) (Clerbaux & Dewitte, 1999). Additional fields contained within the product include shortwave and longwave broad-band radiative fluxes derived from the radiances, scene identification, and information pertaining to the instrument and solar geometry. The product is produced at the SEVIRI acquisition time and has a spatial resolution of 3 × 3 SEVIRI pixels (~ 10 × 10 km at nadir).

2.2. Sampling (cloud and glint identification)

Two cloud flags are provided within the GL2A product. The first, derived routinely at RMIB, employs the visible SEVIRI channels only to distinguish between clear and cloudy conditions (Ipe et al., 2004). The second, produced operationally at EUMETSAT by the Meteorological Products Extraction Facility (MPEF), additionally uses information from the infra-red SEVIRI channels to perform the clear/cloud separation (Lutz, 1999). Both approaches can misclassify dust aerosol as cloud. Brindley & Russel (2006, submitted for publication) developed a dust detection algorithm, and added dusty points back to the nominally clear points given by the MPEF cloud flag. This approach involves using the distinct spectral signature associated with dust aerosol within the infra-red atmospheric window (~ 8–12 μm) to

Table 1
Calibration coefficients for the SEVIRI solar channels over the two periods studied here

Channel (μm)	Calibration coefficients	
	Gain, g (mW m^{-2} sr^{-1} (cm^{-1})$^{-1}$ count^{-1})	Offset, os (mW m^{-2} sr^{-1} (cm^{-1})$^{-1}$)
0.6	0.02295	−1.17046
0.8	0.02922	−1.49001
1.6	0.02328	−1.18724

re-classify points previously considered to be cloudy as dust contaminated. The aerosol retrieval algorithm is then applied to both clear and restored dust pixels. At present, the retrieval domain is limited to points with solar and view zenith angles of less than 60°, following recommendations in Ignatov and Stowe (2002).

To avoid sun-glint, retrievals are not performed on regions where the glint cone angle, γ, defined by Eq. (1) is <30°.

$$\cos\gamma = \cos\theta_v \cos\theta_s + \sin\theta_v \sin\theta_s \cos\phi_r \quad (1)$$

where θ_v and θ_s are the instrument viewing and solar zenith angles respectively, and ϕ_r is the relative azimuth angle. The AVHRR NESDIS aerosol sampling differs in two respects: it completely excludes from retrievals the whole solar side of the orbit (i.e., when ϕ_r<90°), and avoids regions where the glint cone angle is <40°. For SEVIRI, this NESDIS screening was deemed to be too restrictive (removed points which were clearly uncontaminated), and was therefore replaced by the revised threshold.

Fig. 2 provides an illustration of how the nominally clear points (where the aerosol retrieval algorithm is applied) are selected for an individual time slot.

2.3. Radiometric definitions for the SEVIRI solar reflectance bands

Channel reflectances, ρ_{ch}, are defined as:

$$\rho_{ch} = \frac{\pi \times L_{ch}}{S_{ch}} \quad (2)$$

Here, L_{ch} is the channel radiance, S_{ch} the incident solar flux at the top of the atmosphere, (TOA), integrated over the appropriate channel filter function, and the subscript refers to the specific SEVIRI channel.

Table 2
Channel integrated incident solar flux at the TOA, S_{ch}, and corresponding integrated channel width, f_{ch}, for the SEVIRI solar channels

Channel (μm)	S_{ch} (W m^{-2})	f_{ch} (cm^{-1})
0.6	121.293	1825.500
0.8	64.020	877.575
1.6	29.514	471.265

Channel integrals are calculated based on information provided for each spectral response function by EUMETSAT at http://www.eumetsat.int/en/index.html. The reference solar spectrum employed to calculate S_{ch} is taken from Neckel and Labs (1984).

Table 3
Characteristics of the various look-up-tables (LUTs) generated for this study

LUT label	Aerosol model employed
3gen	Monomodal, log-normal size distribution (Eq. (3)), purely scattering aerosol (Eq. (4)) (Ignatov and Stowe, 2002)
Opac0	OPAC 'desert' model at 0% relative humidity (Hess et al., 1998)
Des	'Desert-like' aerosol model from Shettle (1984)
Nonspher	Non-spherical dust aerosol model (after Dubovik et al., 2002a,b)

The channel radiance (in mW m^{-2} sr^{-1}) is obtained from the measured counts, C, using:

$$L_{ch} = (C \times g + \text{os}) \times f_{ch} \quad (3)$$

Here g is the calibration gain, os the offset, and f_{ch} the integrated channel width.

Note that no onboard calibration device is available in the SEVIRI solar reflectance bands, and they are calibrated vicariously (Govaerts & Clerici, 2004). The methodology employed involves the comparison of observed TOA reflectances with reference simulations for the same viewing conditions and illumination over stable, bright desert targets. Further comparisons with selected targets located over the ocean surface are also performed to check the consistency and reliability of the results. The values of g and os for each channel are available from the SEVIRI data files. They

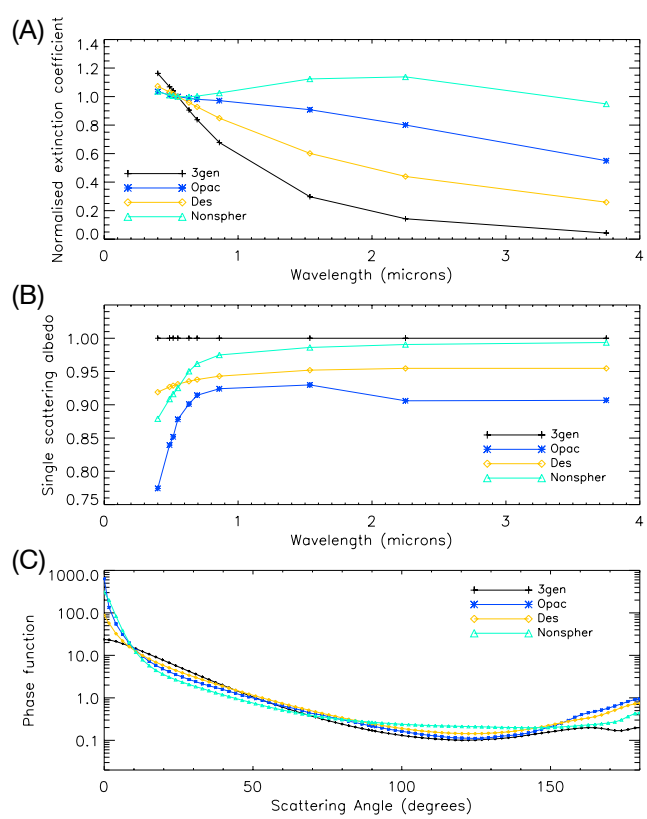

Fig. 3. (A) Spectral dependence of normalized extinction coefficient for 3gen, Opac, Nonspher and Des aerosol models. (B) As (A) for the single-scattering albedo. (C) Dependence of phase function (normalized at 2π) on scattering angle at a wavelength of 0.63 μm for the four aerosol models.

remained constant over the period from March to October 2004 used in this study and are listed in Table 1. Values of S_{ch} and f_{ch} are assumed constant in-flight and are provided in Table 2.

2.4. Generation of reflectance look-up tables

The retrievals are made using pre-calculated, channel specific, look-up tables (LUTs) of reflectances as a function of solar and instrument viewing geometry and aerosol optical depth (Ignatov & Stowe, 2002). Reflectances are calculated for solar and instrument viewing zenith angles ranging from 0° to 84° in steps of 6°, for relative azimuth angles ranging from 0° to 180° in steps of 10°, and for aerosol optical depths (AODs) of 0.0, 0.15, 0.3, 0.6, 0.9, 1.2 and 1.5 for consistency with the original NESDIS settings. Once obtained, these tables are then incorporated in the retrieval algorithm, which essentially consists of a 3-dimensional Lagrangian interpolation designed to locate the optical depth which minimises the difference between the observed and simulated reflectance in a particular SEVIRI channel given the specific solar/view geometry. The original NESDIS algorithm was designed for maritime conditions (generally low AOD) and hence the range of AODs considered may not be appropriate under heavy dust loading. However, to test the expectation that the reflected radiances are approximately linearly dependent on AOD (Griggs, 1975), additional LUTs were specifically generated to span a wider range of values. Employing these LUTs did not result in any statistically significant AOD differences from the values obtained with the generic LUTs reported here.

2.4.1. Aerosol models

Four sets of LUTs are employed in this study, each set comprising three tables derived for the three SEVIRI channels at 0.6, 0.8 and 1.6 μm.

The first set is generated using the 6S radiative transfer model (Vermote et al., 1997a) employed in (Ignatov & Stowe,

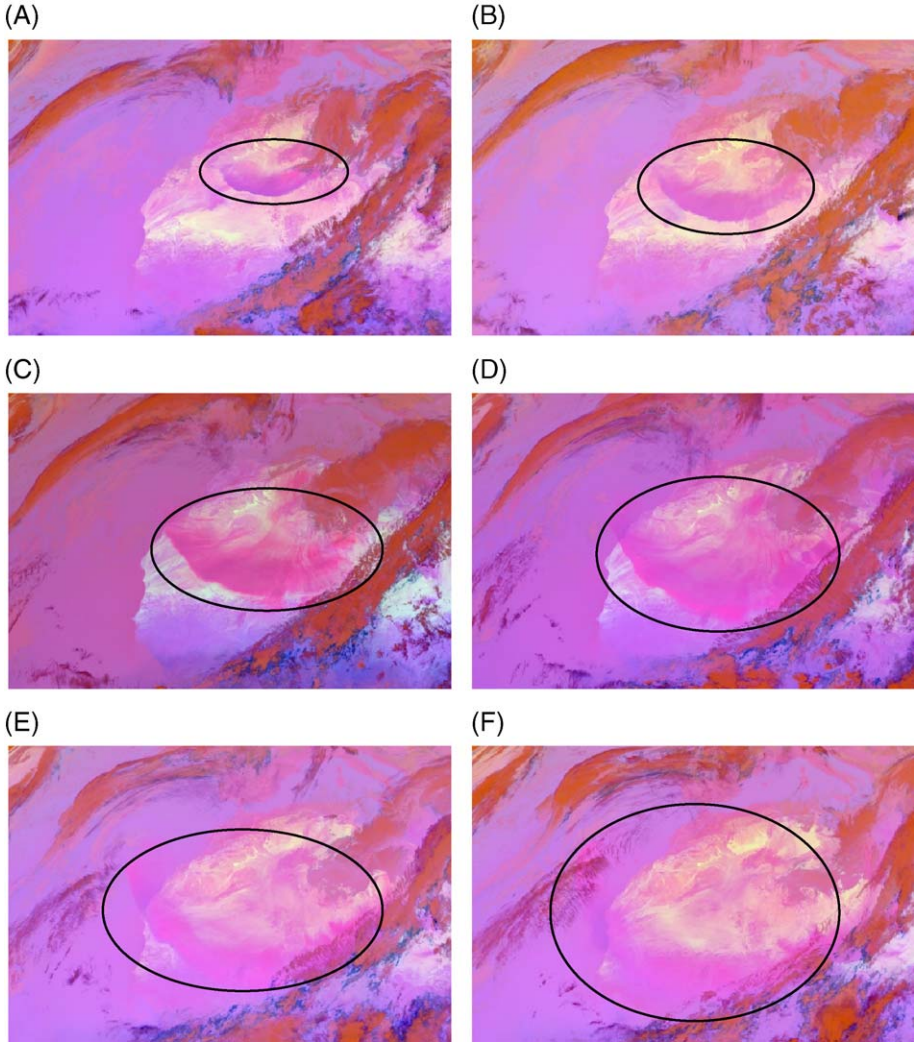

Fig. 4. Six-hourly RGB images showing evolution of dust storm from 00:00 UTC on 3rd March, 2004 to 06:00 UTC on 4th March, 2004. Images are constructed using 12.0–8.7 μm (red), 10.8–8.7 μm (green) and 10.8 μm (blue) infra-red SEVIRI channel brightness temperatures. In each case the position of the dust plume is marked by the black oval.

2002), but taking into account the SEVIRI channels' spectral response functions. The aerosol model has a mono-modal lognormal size distribution:

$$n(R) = \frac{\mathrm{d}N}{\mathrm{d}R} = \frac{1}{R\ln\sigma\sqrt{2\pi}}\exp\left(-\frac{\ln^2\frac{R}{R_\mathrm{m}}}{2\ln^2\sigma}\right) \quad (4)$$

with a mode radius, R_m, of 0.10 μm and a standard deviation, σ, of 2.03. The aerosol is assumed to be purely scattering with a wavelength independent complex index of refraction, n, given by:

$$n = 1.40-0.0i \quad (5)$$

Mie theory is used to generate optical properties for this microphysical model, which are then used in 6S RT calculations. For future reference, aerosol retrievals obtained from the LUTs generated using this model are labelled '3gen'.

Note that the choice of fixed parameters used in the 3rd generation model may not be optimal for dust retrievals. To investigate the impact of a different aerosol model on the retrieved properties, three further sets of LUTs were calculated using 6S. The aerosol models used to generate these LUTs were specifically designed to represent mineral dust and in each case the refractive indices vary with wavelength.

The 2nd set of LUTs (hereafter, Opac) is generated for the aerosol model taken from the Optical Properties of Aerosols and Clouds (OPAC) database (Hess et al., 1998). Use is made of the 'desert' aerosol type, where the aerosol size distribution is assumed to be multimodal lognormal with a maximum and minimum radius of 0.005 and 60 μm respectively. The four modes represent in turn a water soluble (assuming a relative humidity of 0%), mineral nucleation, mineral accumulation and mineral coarse component. The complex refractive index of the water soluble component at 0.55 μm is given by:

$$n = 1.53-0.006i \quad (6)$$

while the complex refractive index of all the mineral components at 0.55 μm is given by:

$$n = 1.53-0.0055i \quad (7)$$

Optical properties are calculated using Mie theory for each component, and then combined using:

$$x = \sum_i x_i^1 N_i \quad (8)$$

where x is the desired optical property representative of the whole aerosol mixture, x_i^1 is the value of the property for each

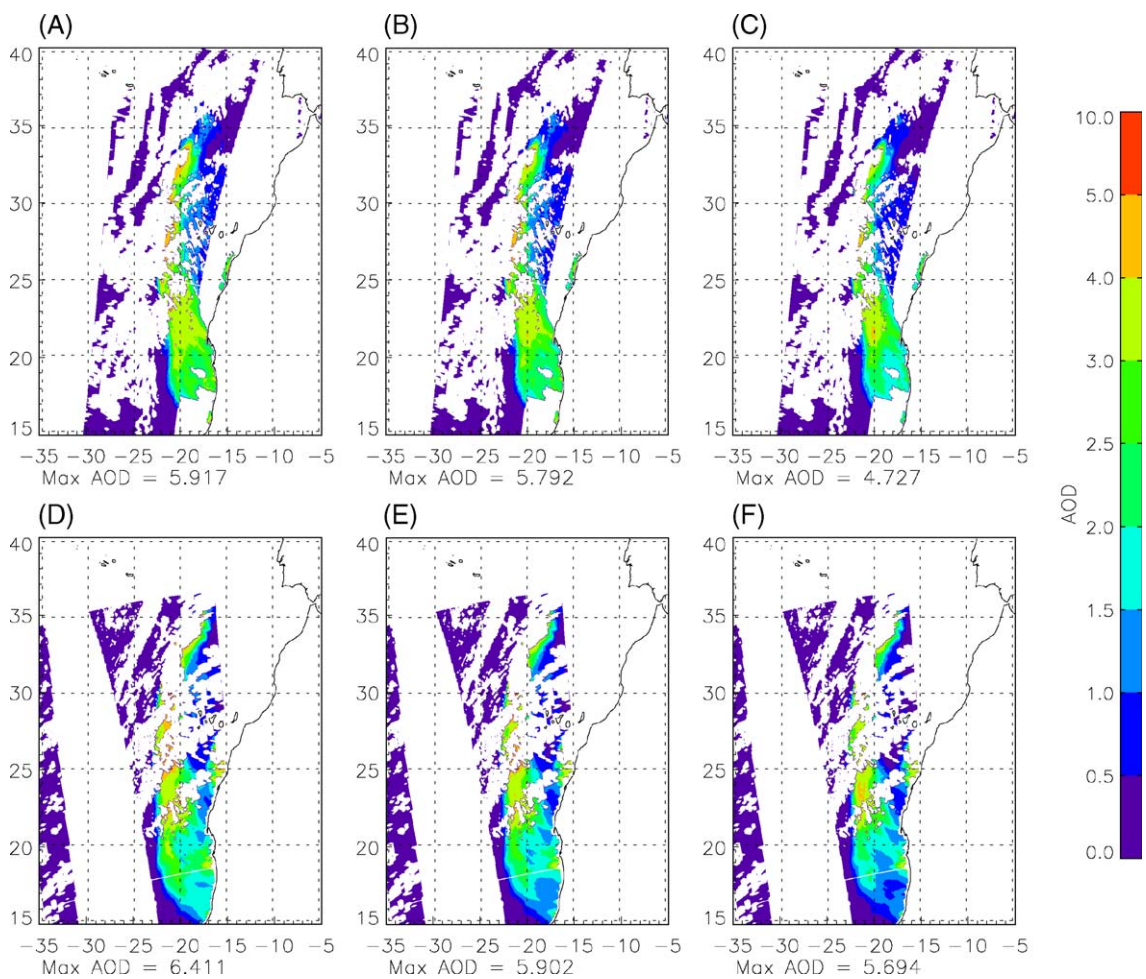

Fig. 5. Top row: AOD at (A) 0.644 μm; (B) 0.855 μm; (C) 1.632 μm derived from two 5-min granules of *Terra*/MODIS data from 11:50–12:00 UTC on March 4th 2004. Middle row (D–F): As top row, but derived approximately 3 h later from two 5-min granules of *Aqua*/MODIS data taken between 14:55–15:05 UTC.

component of the mixture normalized to a number density of 1 particle cm^{-3}, and N_i is the number density of the given component in particles cm^{-3}.

The 3rd set of LUTs (hereafter, Des) employs the 'desert-like' dust aerosol model due to Shettle (1984) (note that this model is also included as a default aerosol representation in the 6S code, Vermote et al., 1997a).

All of the above aerosol models assume particle sphericity, which may well be inappropriate for dust particles (Mishchenko et al., 1995). To investigate the impact that non-sphericity may have on the SEVIRI retrieval quality a 4th set of LUTs (hereafter, Nonspher) was generated from aerosol optical properties obtained using the approach described in Dubovik et al. (2002a). This assumed that the dust particles were randomly orientated spheroids, with a size distribution and spectral refractive index based on AERONET dust retrievals (Dubovik et al., 2002b). Similar non-spherical models have been tested with aerosol retrievals from the Geostationary Operational Environmental Satellite-8 Imager (Wang et al., 2003) and NOAA/AVHRR (Zhao et al., 2003).

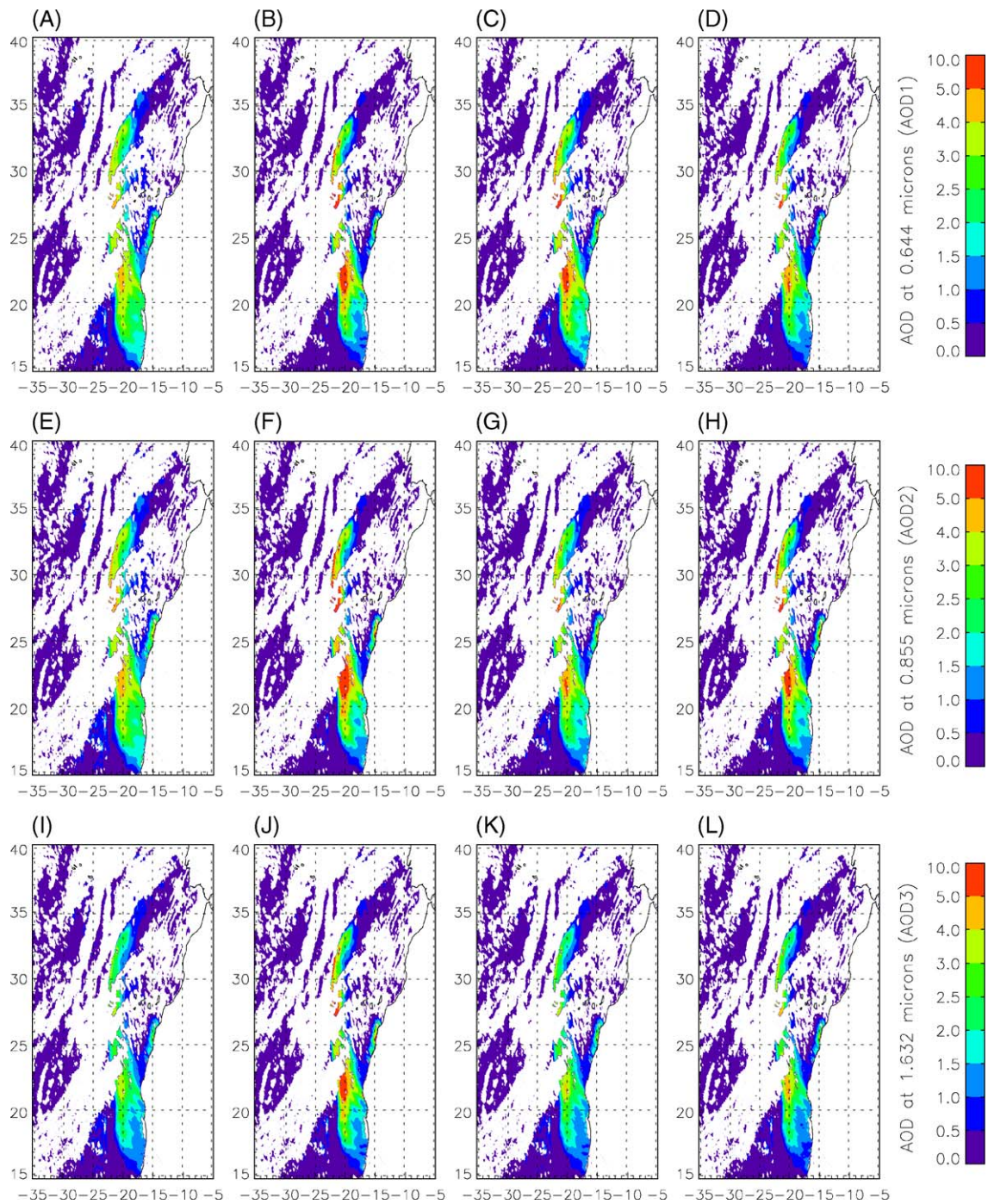

Fig. 6. Top row: AOD at 0.644 μm (band 1) derived from SEVIRI observations at 12:00 UTC on 4th March 2004 using (A) NESDIS 3gen LUTs; (B) Opac LUTs; (C) Nonspher LUTs; (D) Des LUTs. Middle row: As top row but for AOD at 0.855 μm (band 2). Bottom row: As top row but for AOD at 1.632 μm (band 3).

A summary of the all the LUTs generated in the course of this study is provided in Table 3. Fig. 3(A) shows the extinction coefficient as a function of wavelength (normalised to 0.55 μm) for the four different aerosol models introduced above, while the spectral dependence of the single-scattering albedo associated with each model is shown in Fig. 3(B). Fig. 3(C) indicates the dependence of the phase function on scattering angle for a wavelength of 0.63 μm.

Focussing initially on the dust specific aerosol representations, the inclusion of additional larger modes in the Opac, Des and Nonspher size distributions result in a reduction in the spectral dependency of the extinction coefficient compared to the generic 3gen model. Above 0.6 μm, the non-spherical model shows reduced absorption relative to the other two dust specific representations. In terms of the aerosol phase function, both the Opac and desert-like models generally show higher values than those seen in the generic model, except in the region between 10° and 50°. Particularly striking is the much stronger forward scattering peak, and a noticeably different angular dependency in the back-scatter region at scattering angles greater than 150°.

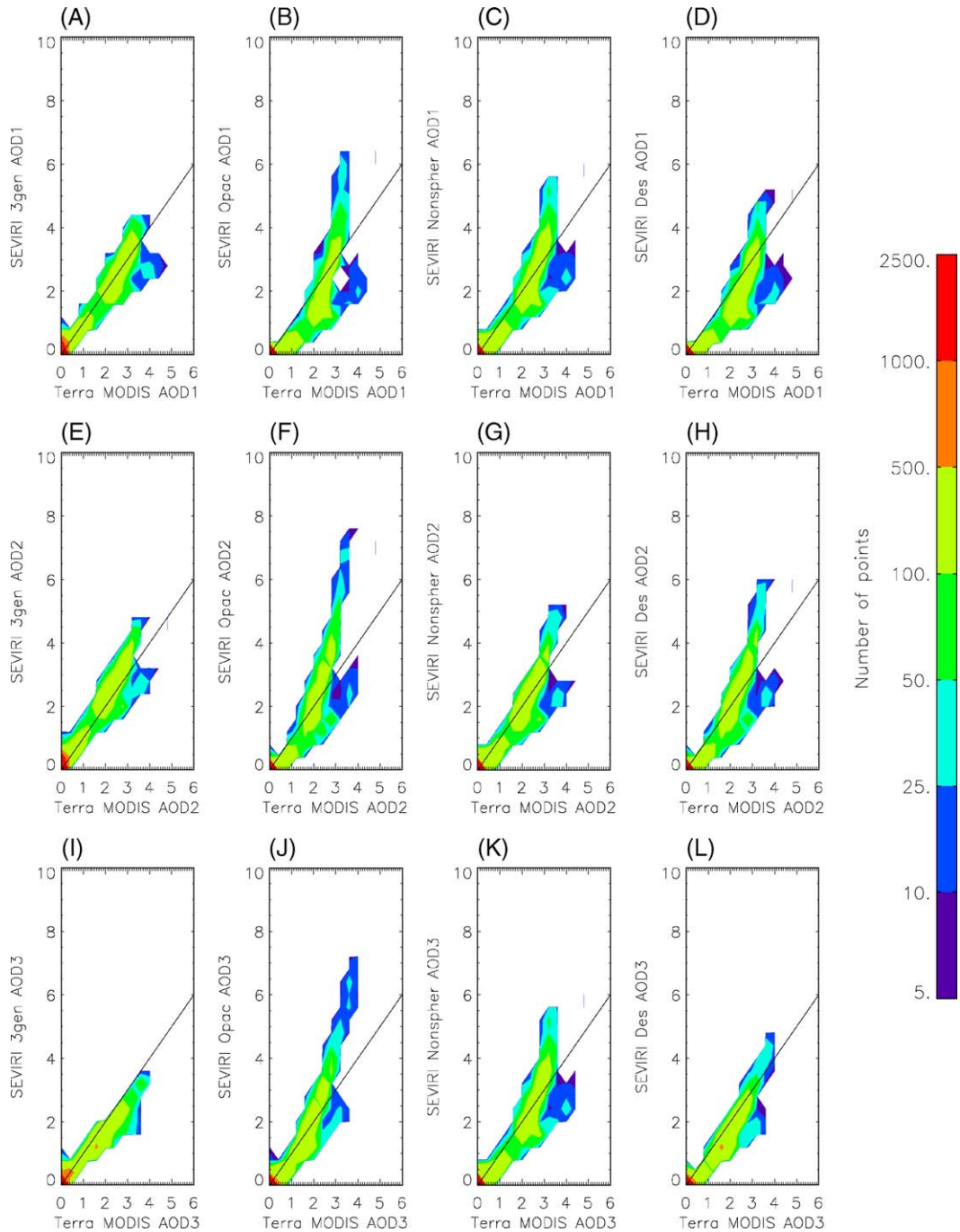

Fig. 7. SEVIRI versus *Terra*/MODIS AOD comparison statistics derived from Figs. 5 and 6. Top row: Density scatter plots of top row of Fig. 6 versus Fig. 5(A). Middle row: As top row but for middle row of Fig. 6 versus Fig. 5 (B). Bottom row: As top row but for bottom row of Fig. 6 versus Fig. 5 (C). Note that AOD1 refers to the retrieval in band 1, AOD2 to band 2 and AOD3 to band 3.

Similar relative behaviour is shown by the non-spherical case, although the variation with angle is much flatter than that seen in all of the other representations between ~30° and 160°. A slight increase with angle is seen between 160° and 180°, although it is substantially smaller than that seen in either the Opac or Des models. The Meteosat-8 platform is well suited to evaluate these differences in the phase functions in terms of their effect on AOD because the sun-SEVIRI relative geometry progresses through a wide range of scattering angles during the course of a day.

2.4.2. Sea-surface contribution

In the 6S code the sea-surface reflectance, ρ_{sfc}, comprises contributions from whitecaps, (ρ_{wc}), underlight, (ρ_{sw}), and ocean glint, (ρ_{gl}), (Vermote et al., 1997b), such that:

$$\rho_{sfc}(\theta_s, \theta_v, \phi, \lambda) = \rho_{wc}(\lambda) + (1-\rho_{wc}(\lambda) \times \rho_{sw}(\theta_s, \theta_v, \phi, \lambda) + (1-f) \times \rho_{gl}(\theta_s, \theta_v, \phi, \lambda) \quad (9)$$

where f is the relative area covered by whitecaps and is calculated using:

$$f = 2.95 \times 10^{-6} \times w^{3.52} \quad (10)$$

and w is the surface wind speed in m s^{-1} (Monahan & Muircheartaigh, 1980). The LUTs used here employ this surface representation, but consider both the whitecap and underlight components to be Lambertian in nature with a fixed joint contribution specific to each spectral channel (see Ignatov & Stowe, 2002 for full details). The simulations use a wind speed of 1 m s^{-1}, and the built in anisotropic bi-directional glint reflectance model. Essentially the reflectance model becomes:

$$\rho_{sfc}(\theta_s, \theta_v, \phi, \lambda) = \rho_{gl}(\theta_s, \theta_v, \phi, \lambda) + \rho_{diff}(\mathrm{ch}) \quad (11)$$

where ρ_{diff}(ch) is the diffuse reflectance for each SEVIRI channel, and is considered constant across the given channel wavelength range. The values employed for each band are: 0.002 (0.6 μm: band 1), 0.0005 (0.8 μm: band 2) and 0.0 (1.6 μm: band 3).

It should be noted that these "open ocean" (or Case 1) surface reflectance values, and their corresponding uncertainties, are equivalent to a few hundredths AOD, at the maximum, and errors may be proportionately larger over Case 2 turbid waters (Ignatov & Stowe, 2002). For the analyses in this study, however, when typical AODs exceed 1, the surface reflectance induced errors are deemed to be a non-significant source of AOD errors.

2.5. Output quantities

Regardless of the origin of the LUTs employed within the retrieval algorithm, the output quantities are the channel specific aerosol optical depths, δ_i, reported at three monochromatic reference wavelengths of λ_1=0.630, λ_2=0.830, and λ_3=1.610 μm. Note that the sensor bands have finite widths and are (slightly) displaced with respect to the reference wavelengths. The retrieval therefore involves some scaling and/or spectral extrapolation, whose effect on the retrieved AOD does not exceed a few percent (Ignatov & Stowe, 2002).

Table 4
Mean AOD differences "SEVIRI minus MODIS" for the 3gen, Opac, Des and Nonspher LUTs on 5 March 2004

Satellite/time	Channel (μm)	Aerosol model	Mean	SD	Min	Max
Terra 11:50–12:00 UTC	0.644	3gen	0.024	0.346	−2.357	1.558
		Opac	−0.161	0.644	−3.063	3.665
		Nonspher	−0.017	0.495	−2.557	2.846
		Des	−0.239	0.489	−3.025	2.134
	0.855	3gen	0.165	0.320	−1.904	1.725
		Opac	0.084	0.710	−2.351	4.464
		Nonspher	−0.022	0.392	−2.436	2.075
		Des	−0.016	0.507	−2.408	3.038
	1.632	3gen	−0.088	0.305	−2.654	1.417
		Opac	0.067	0.529	−2.763	3.735
		Nonspher	−0.118	0.294	−2.380	1.281
		Des	−0.129	0.311	−2.772	1.343
Aqua 14:55–15:05 UTC	0.644	3gen	0.068	0.340	−3.048	1.373
		Opac	1.222	2.094	−1.774	13.506
		Nonspher	0.242	0.569	−2.945	3.938
		Des	0.328	0.635	−2.818	4.377
	0.855	3gen	0.203	0.290	−2.475	1.558
		Opac	1.003	1.549	−1.504	10.359
		Nonspher	0.247	0.420	−2.486	2.817
		Des	0.493	0.751	−2.186	5.347
	1.632	3gen	−0.020	0.348	−3.131	1.127
		Opac	0.528	0.844	−2.544	6.048
		Nonspher	0.057	0.301	−3.045	1.259
		Des	0.172	0.348	−2.938	2.275

The associated standard deviation (SD) and range of differences is also provided. (Statistics calculated from data in Figs. 7 and 8.).

In addition to AODs, the ratio from different channels can be used to infer the Ångström exponent (AE), α, of the observed aerosol using:

$$\alpha_{ij} = -\frac{\ln \frac{\tau_{\lambda_i}}{\tau_{\lambda_j}}}{\ln \frac{\lambda_i}{\lambda_j}}, \quad (12)$$

where $\tau_{\lambda i}$ and $\tau_{\lambda j}$ are the retrieved optical depths at wavelengths λ_i and λ_j respectively. The α calculated in this manner is not the same as that which would be obtained from the ratio of the extinction coefficients for the specific aerosol model used to derive τ. Provided the model is not too far from the truth, then the α given by Eq. (12) will be more representative of the actual aerosol than that given by replacing the retrieved τs with the model extinction coefficients (see Ignatov and Stowe (2000) for a more detailed discussion). However, if the assumed aerosol model deviates strongly from the true aerosol behaviour then this may not be the case (Fig. 10 clearly illustrates this later in the text).

Although the calculations used to derive the LUTs from which the aerosol optical depths are retrieved specifically use the SEVIRI channel filters, it is possible to use Eq. (12) together with the specific aerosol model employed within the LUT to scale the results to alternative wavelengths in order to

allow comparisons with values obtained from other sources. Rearranging:

$$\tau_{\lambda_{\mathrm{ref}}} = \tau_1 \left(\frac{\lambda_1}{\lambda_{\mathrm{ref}}} \right)^{\alpha} \tag{13}$$

where $\tau_{\lambda\mathrm{ref}}$ is the optical depth at the reference wavelength λ_{ref}. Because the 6S LUTs were designed to provide a direct comparison with AVHRR retrievals the reference wavelengths at which optical depths are reported are 0.63, 0.83 and 1.61 μm. When alternative reference wavelengths are considered this will be stated explicitly.

The results presented in this study were obtained by running the retrieval code in a stand alone mode. However, efforts are now underway to incorporate a real-time version within the GERB processing scheme.

3. Application to SEVIRI observations

The retrieval procedure is tested below with two case studies. Both are fairly substantial dust events in terms of magnitude, and both show a significant variation in their diurnal AOD signal (see Sections 3.1.1 and 3.2.1). Nevertheless it should be

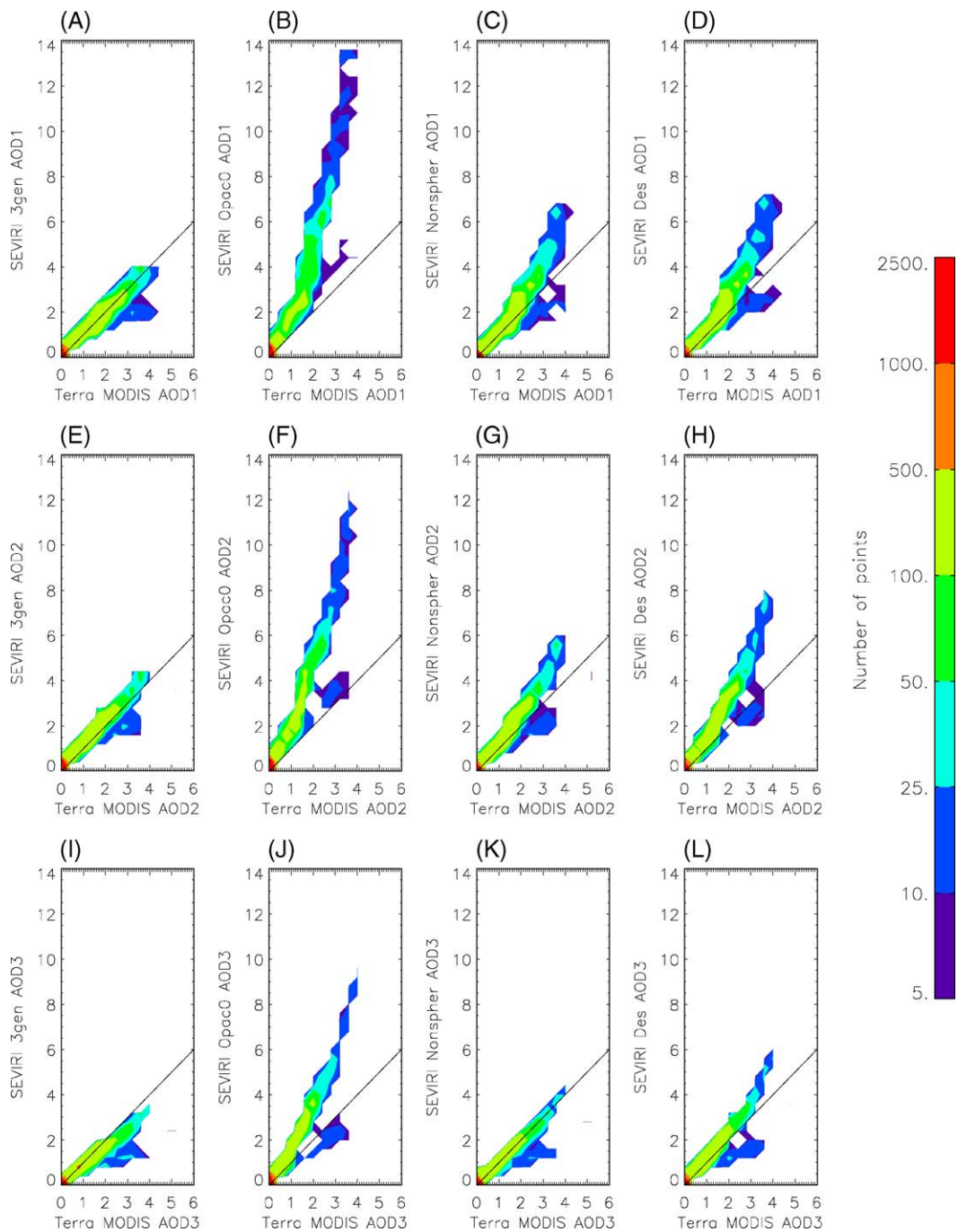

Fig. 8. As Fig. 7 but comparing the SEVIRI and *Aqua*/MODIS observations around 15:00 UTC.

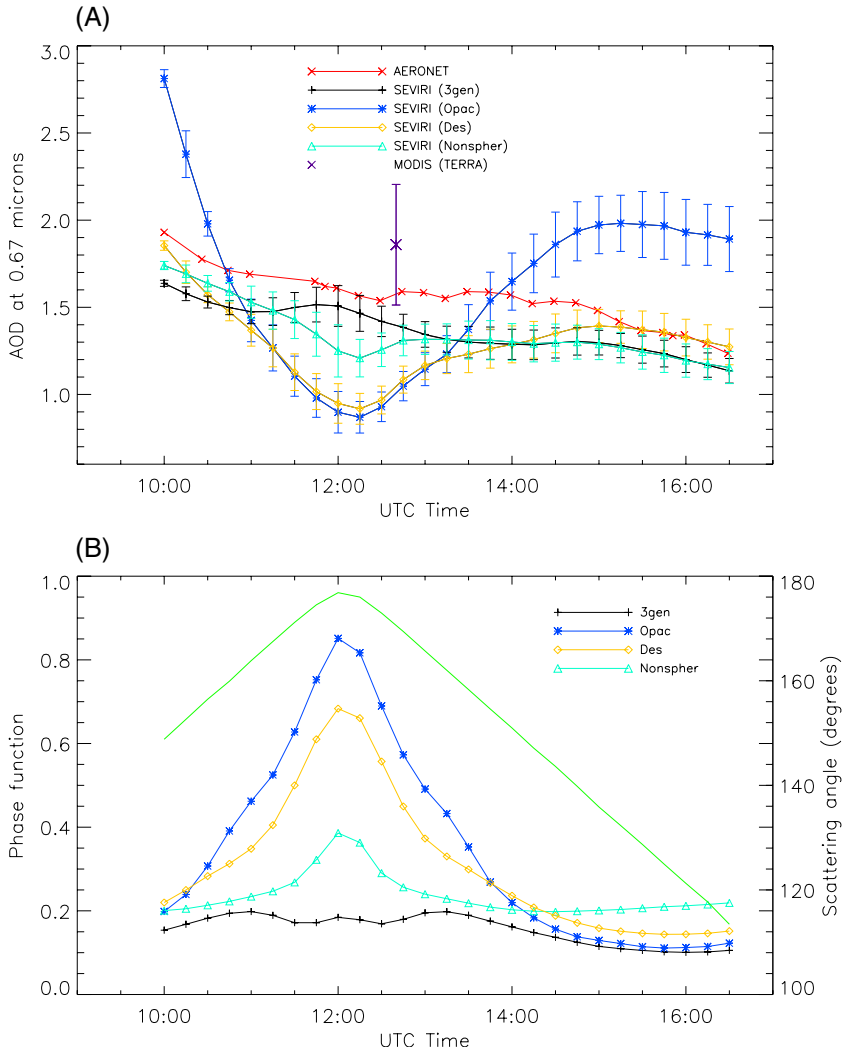

Fig. 9. (A) Time-series of AODs at 0.67 μm through 5 March, 2004 from AERONET Capo Verde station (16.72°N 22.93°W). Corresponding retrievals from SEVIRI using the Opac, Nonspher, Des and 3gen LUTs are also shown, along with the *Terra*/MODIS AOD at 12:40 UTC. (Note that *Aqua*/MODIS does not sample the Capo Verde aerosol site on this day.) In each case the optical depths from SEVIRI and MODIS have been scaled from the retrieval wavelengths of 0.63 and 0.644 μm to the AERONET wavelength of 0.67 μm. The one standard deviation spread due to the spatial variability in the SEVIRI retrieved optical depths is indicated in each case by the vertical bars. (B) Dependence of scattering angle of SEVIRI observations on time over the same day (green line). Values of the phase function at the given scattering angle for each of the aerosol models used in (A) are also shown.

noted that previous work has shown that climatological daily average values of dust loading can be adequately obtained from instruments in polar orbit (Kaufman et al., 2000). The first event considered here is a large dust storm which took place from March 3rd–5th, 2004. The second is a smaller dust outbreak seen just off the coast of Senegal during October 12th–13th 2004. Each event is discussed in turn below.

3.1. Case-study 1: 3rd–5th March, 2004

Fig. 4(A–F) are six-hourly SEVIRI composite images which track the evolution and spread of the dust storm from 00:00 UTC on the 3rd March through to 06:00 UTC on the 4th. The composites are made up of contributions from the different SEVIRI infra-red window channel brightness temperatures with the position of the dust plume picked out by the black oval. The increase in the dust extent with time from its fairly localised origin over southern Algeria is striking, with the plume affecting conditions not only over the whole of the north-west African continent, but also well out over the north Atlantic by 06:00 UTC on the 4th March, a situation which is perpetuated over the next thirty-six hours.

3.1.1. Aerosol optical depth

Fig. 5 shows MODIS AOD retrievals in the three "SEVIRI-like" spectral bands on the 4 March 2004 derived from two 5-min MOD04/*Terra* granules from 11:50–12:00 UTC (top) and from two 5-min MYD04/*Aqua* granules from 14:55–15:05 UTC (bottom). The dust sheet is clearly delineated in all three bands from both platforms, extending out over the Atlantic from the north-west coast of Africa, with optical depths reaching maximum values of up to 6.4 at the later time in the 0.644 μm band. Comparison of these *Terra* and *Aqua* snapshots, separated in time by approximately 3 h,

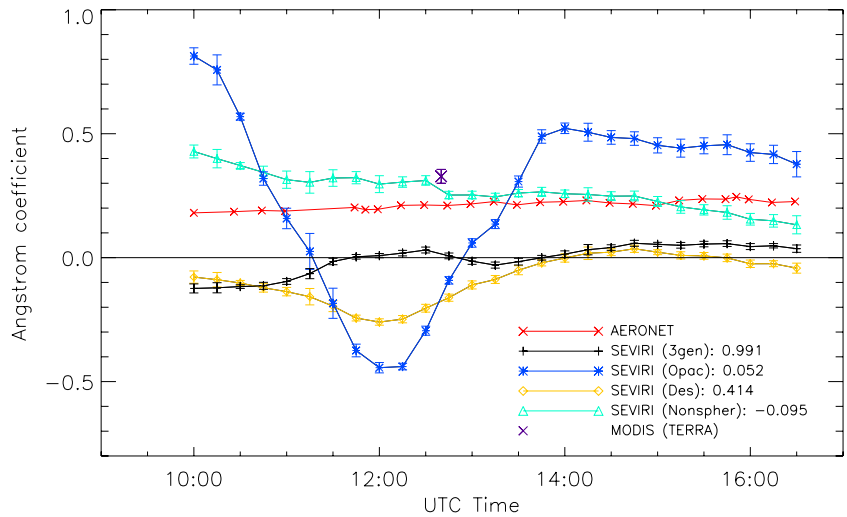

Fig. 10. Temporal evolution of the Angstrom exponent on 5 March 2004 over the Capo Verde site as derived from AERONET observations and SEVIRI retrievals based on the Opac, Des, 3gen and Nonspher LUTs. The spread in the calculated AEs due to the spatial variability in the retrieved SEVIRI optical depths is indicated by the vertical bars. The available *Terra*/MODIS value at 12:40 UTC is also shown for comparison. The numbers associated with each SEVIRI trace in the legend are the AE which would be obtained if calculated using the extinction coefficients specific to each model (see text for further details).

provides an illustration of the temporal dynamics of the aerosol field.

For comparison with the *Terra*/MODIS results in Fig. 5, the top row of Fig. 6 shows the distribution of AODs retrieved from SEVIRI band 1 (scaled from the retrieval wavelength of 0.630 μm to the MODIS central wavelength of 0.644 μm as described in Ignatov et al., 2005) at 12:00 UTC using each of the four LUTs described in Section 2. The middle and bottom rows show the same information derived from SEVIRI band 2 (scaled from 0.830 to 0.855 μm) and band 3 (scaled from 1.610 to 1.632 μm) respectively. In all four cases the AOD pattern is broadly similar to that seen in the *Terra*/MODIS retrievals. However, on closer inspection there are systematic differences between the various sets of SEVIRI retrievals due to the specific aerosol model employed in the LUT generation.

Fig. 7 shows density plots of SEVIRI AODs for the three bands and four aerosol models against those retrieved from *Terra*/MODIS and Table 4 summarises the respective comparison statistics. SEVIRI AODs tend to be biased low with respect to MODIS in the main body of the dust sheet, but this trend is reversed towards the northern edge of the plume (not shown). Both the figures and the table indicate that the deviations of SEVIRI retrievals from MODIS are smallest for the NESDIS 3gen algorithm and largest for the Opac case, with the Des and Nonspher cases falling in between these two extremes. Note that MODIS and SEVIRI retrievals are available in somewhat different domains, due to differences in their respective view geometry, and cloud and glint masks. These sampling differences however should not affect the MODIS/SEVIRI comparisons in their intersection sample where both retrievals are available, used for plotting Fig. 7.

In the 6S code, gaseous absorption is assumed to occur entirely above the scattering layer. Violation of this assumption (e.g. when the dust is lofted above the boundary layer) may potentially cause a low bias in the 6S reflectances, which in turn results in a high bias in the retrieved AOD. As SEVIRI channel 2 is sensitive to water vapour it will be most affected by this 6S limitation. Indeed, the middle row of Fig. 7(E–H) may suggest a slight positive bias in the SEVIRI AOD with respect to MODIS, compared to the other two bands shown in the top and bottom rows.

To assess whether the results seen in Fig. 7 are consistent through the day, Fig. 8 shows corresponding density plots obtained three hours later, at 15:00 UTC. While the 3gen versus *Terra*/MODIS mean optical depth relationship seen at 12:00 UTC are preserved (the first column of Fig. 8), the corresponding Opac and Des comparisons now show a marked tendency to overestimate the AOD throughout the whole observed range. In contrast, the Nonspher model shows a pattern of behaviour which is consistent with that seen at 12:00 UTC in bands 1 and 2, but the level of agreement with the MODIS retrievals is significantly improved in band 3. Further details of the difference range, the mean value and its associated standard deviation for each comparison are provided in Table 4.

Comparison with MODIS provides a good consistency check for the SEVIRI retrievals, however the MODIS data itself may be subject to errors, especially in dusty cases (e.g. Remer et al. (2005) and references therein). Comparison with ground-based sun-photometers provides a more direct means of assessing the accuracy of the SEVIRI AODs. Also, given the wide spread among the four SEVIRI retrievals, and the changes seen between the two MODIS observation times, additional analyses are required to establish the cause of these AOD differences. Measurements at the Capo Verde AERONET site based on Sal Island (16.72°N, 22.93°W) lend themselves to validation of the SEVIRI and MODIS retrievals, and more importantly, to a more complete assessment of the time dependent behaviour of all the models. Since the retrieval algorithm is at present designed to work over ocean only, the point AERONET observations are compared to SEVIRI quantities averaged over the nearest available ocean pixels. For Sal this comprises eight pixels either side of the island, covering a total area of approximately 60 km^2. When comparisons are presented

graphically later in the text, the standard deviations of the averages are also shown to indicate the spatial variability of the SEVIRI retrievals.

Fig. 9(A) illustrates the temporal variation of the SEVIRI retrieved 0.6 μm channel AOD over March 5th as obtained using the Opac, Des, Nonspher and 3gen aerosol representations over the Capo Verde site. The corresponding ground based observations are also shown; in each case the SEVIRI AOD has been scaled to match the nearest AERONET wavelength of 0.67 μm. For completeness, the average of the available *Terra*/MODIS retrievals located within ± 1° longitude and latitude of the Sal site at 12:40 UTC, scaled to 0.67 μm, is also superimposed. Note that complementary MODIS retrievals from *Aqua* were not available within the required geographical

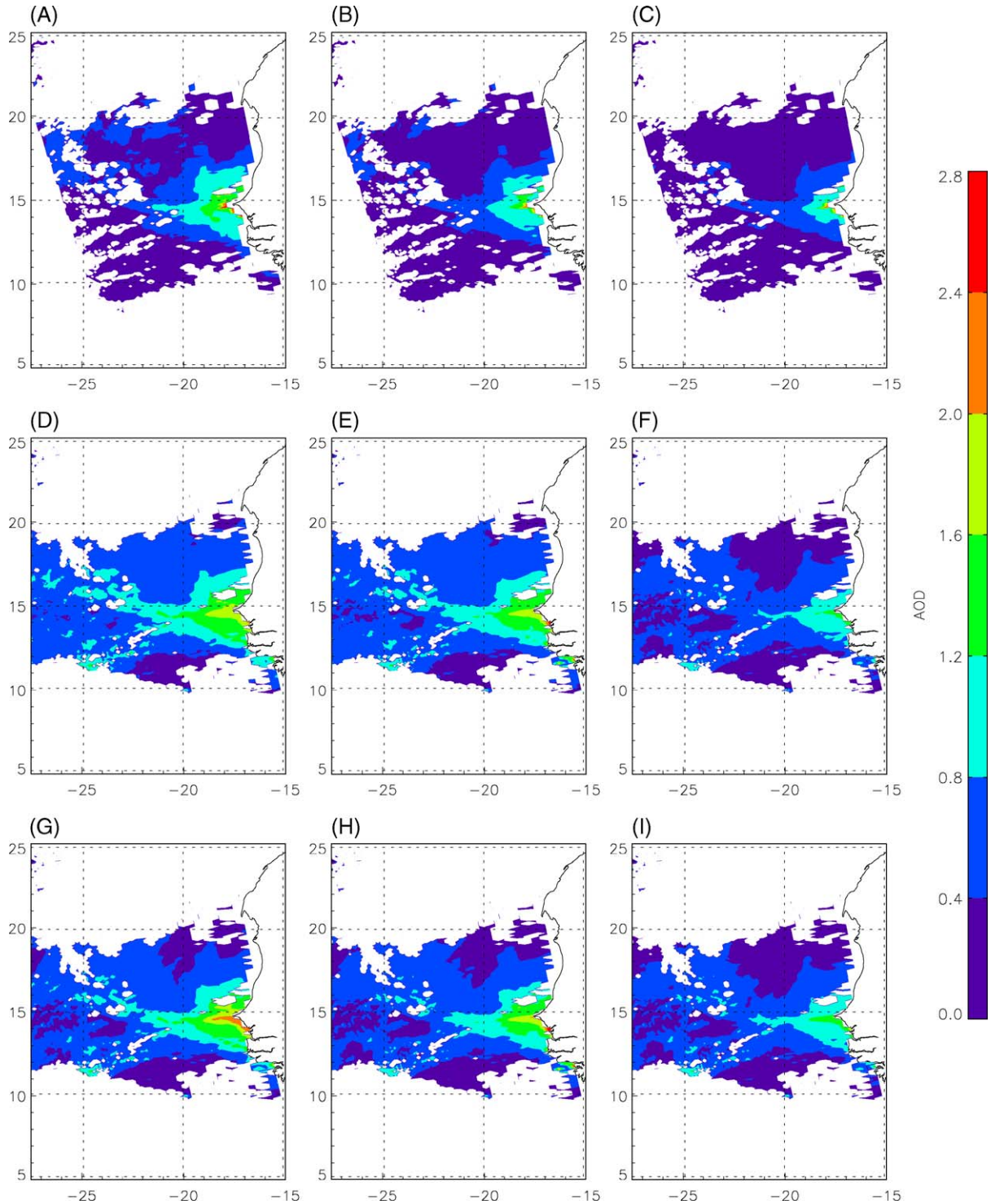

Fig. 11. Top row: AOD derived from one 5-minute *Aqua*/MODIS granule taken between 15:10–15:15 UTC on 12th October 2004 at (A) 0.644 μm; (B) 0.855 μm; (C) 1.632 μm. Middle row: As top row but AOD derived from SEVIRI observations at 15:15 UTC on 12th October 2004 using the 3gen LUTs. Bottom row: As middle row, but AODs derived from SEVIRI observations using Nonspher LUTs.

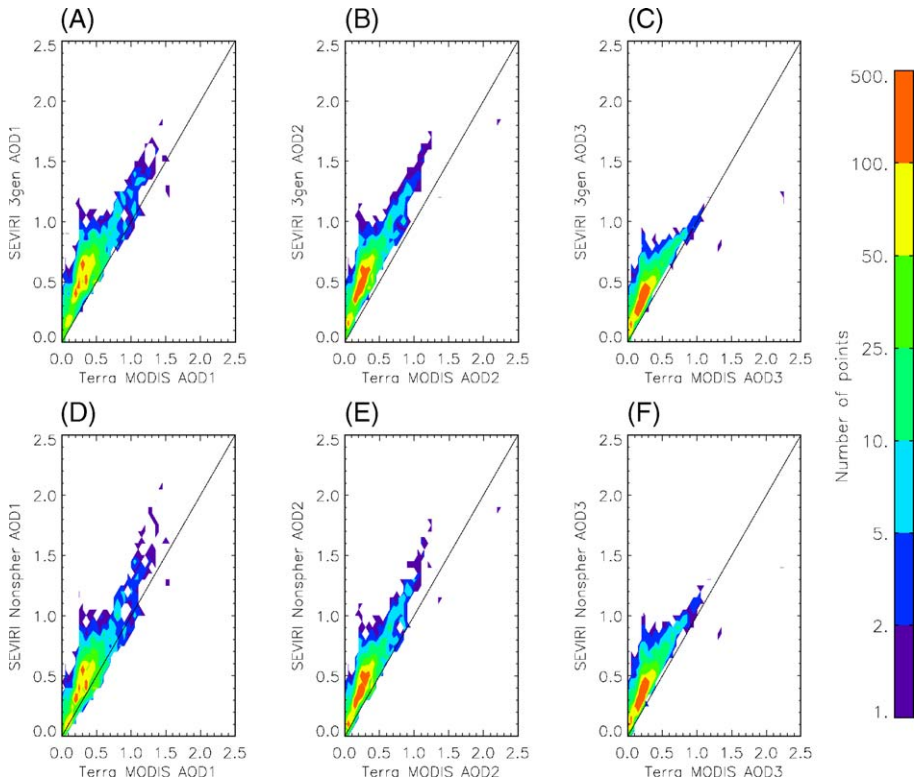

Fig. 12. SEVIRI versus *Aqua*/MODIS AOD comparison statistics derived from Fig. 11. Top row: Density scatter plots of top versus middle row of Fig. 11. Middle row: As top row but for top versus bottom row of Fig. 11.

constraints since the instrument swath width did not encompass Sal Island.

The lack of agreement with the AERONET observations (in both the temporal behaviour of the AOD and its magnitude) is most clearly apparent in the Opac retrievals. Indeed, to mimic the evolution of the Opac curve the dust plume would have had to fan out over the island, contract back to the east, and then move west again, an unlikely scenario, and one which is clearly not seen in the earlier imagery (Fig. 4(A–D)). The Des retrievals show a similar pattern of unrealistic temporal behaviour. In contrast to these models, the retrievals obtained using both the 3gen and Nonspher representations are much more consistent with both the AERONET observations and the expected movement of the plume from east to west over the island. However, it should be noted that both sets of AODs are biased systematically low with respect to AERONET by 0.1–0.2. The reason for this close to systematic 10–15% underestimate is not immediately clear but it may be related to aerosol absorption, which is not accounted for at all in the 3gen model, and is relatively low in the Nonspher representation (single scattering albedo ~ 0.97 at 0.67 μm).

The differences between the four SEVIRI curves in Fig. 9(A), can be explained using a linearized single-scattering approximation, where the aerosol path radiance (i.e., radiance measured by the satellite sensor corrected for gaseous absorption and contributions from Rayleigh scattering and oceanic reflectance) is proportional to a product of aerosol optical depth, phase function, and single scattering albedo (e.g. Gordon and Morel, 1983; Viollier et al., 1980). Fig. 3(C) shows that the NESDIS phase function is relatively flat in the backscatter region (i.e., at scattering angles $\chi > 120°$) whereas the two spherical dust phase functions form a coherent and significantly different cluster, with the strongest divergence between the two groups taking place at $\chi > 150°$. The Nonspher phase function falls between these two patterns of behaviour at $\chi > 150°$, while showing the lowest variability with scattering angle for $120° < \chi < 150°$.

Fig. 9(B) plots time series of χ for the SEVIRI solar/viewing geometry, together with the corresponding aerosol model phase functions over the Capo Verde site. The 3gen and Nonspher phase functions are relatively stable over the course

Table 5
Mean AOD differences "SEVIRI minus MODIS" for the 3gen and Nonspher LUTs at 0.644, 0.855 and 1.632 μm on 12 October 2004

Satellite/time	Channel (μm)	Aerosol model	Mean	SD	Min	Max
Terra 12:05–12:10 UTC	0.644	3gen	0.092	0.155	−0.236	0.863
		Nonspher	0.016	0.149	−0.316	0.789
	0.855	3gen	0.146	0.133	−0.123	0.897
		Nonspher	0.054	0.124	−0.223	0.750
	1.632	3gen	0.116	0.120	−0.144	0.827
		Nonspher	0.107	0.124	−0.150	0.866
Aqua 15:10–15:15 UTC	0.644	3gen	0.214	0.143	−0.894	0.956
		Nonspher	0.137	0.141	−0.756	0.957
	0.855	3gen	0.248	0.123	−0.652	0.916
		Nonspher	0.165	0.118	−0.608	0.857
	1.632	3gen	0.157	0.108	−1.204	0.985
		Nonspher	0.163	0.113	−1.074	1.096

The associated standard deviation (SD) and range of differences is also provided. (Statistics calculated from data in Fig. 12.).

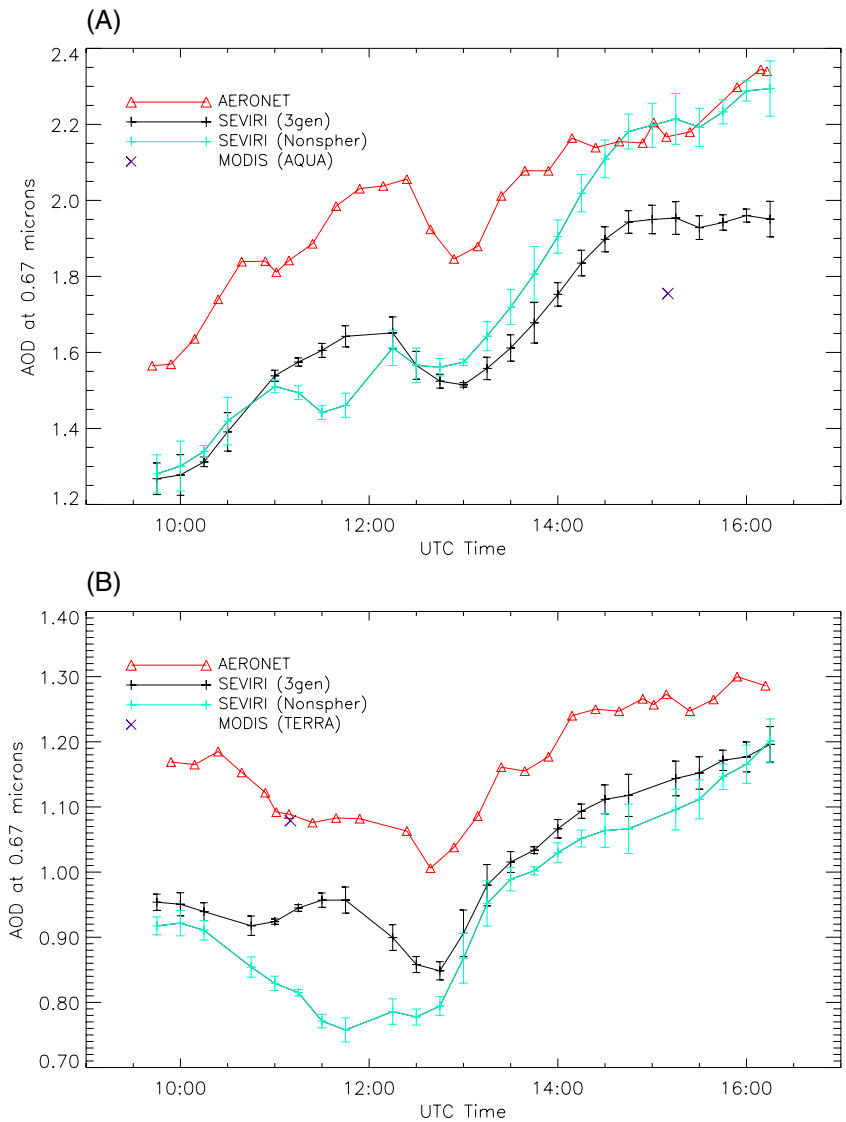

Fig. 13. Temporal evolution of 0.67 μm AOD over the Dakar site (14.38°N, 16.95°W) from AERONET observations and retrieved from SEVIRI using 3gen and Nonspher LUTs for (A) 12th October, 2004; (B) 13th October, 2004. Available MODIS observations are also indicated (note that the *Terra* (*Aqua*) observation on 12th (13th) October lies within the MODIS sun-glint mask). MODIS and SEVIRI observations have been scaled to 0.67 μm to facilitate comparisons, and the one standard deviation spread due to the spatial variability in the SEVIRI retrieved optical depths is indicated by the vertical bars.

of the day, whereas the other two phase functions change by a factor of ~4: first increasing from 10:00 to 12:00 UTC, and then decreasing in the afternoon. The retrieved AODs basically mirror the phase function curves: the retrieved Opac and Des AODs show a pronounced minimum around 12:15 UTC, a feature related to the strong increase in the phase functions of these models with increasing χ. In contrast, the 3gen and Nonspher AOD curves show a much reduced χ-dependency at these angles, consistent with the reduced variation in the appropriate phase function.

3.1.2. Ångström exponent (AE)

Fig. 10 shows time series of the AE, calculated by applying Eq. (12) to the AODs retrieved from SEVIRI in bands 1 and 2, for each aerosol model. The corresponding AERONET values are also provided for comparison. Similar to the AERONET AE, the 3gen AE is relatively flat as a function of time but is biased low by ~ 0.2–0.3. The Nonspher AE also shows a relatively small dependence on time but provides a better match to the magnitude of the AERONET observations. Moving to the spherical dust-like models, the Des AEs are similar to their 3gen counterparts, but show slightly enhanced structure with time, while the Opac values are clearly completely unrealistic. This provides an illustration of the effect of using Eq. (12) to derive AE when the assumed aerosol model is substantially different to the true, observed aerosol. The numerical values next to each SEVIRI caption in the legend are those that would be obtained by using the given aerosol model extinction coefficients to derive AE. Clearly, for the Nonspher and 3gen models, the use of Eq. (12) provides an improved estimate. The spread in the calculated SEVIRI AE values resulting from the spatial variability in the retrieved optical depths is indicated by the vertical bars on each point. The mean AE value derived from the 0.644 and 0.855 μm *Terra*/MODIS AOD retrievals indicated in the

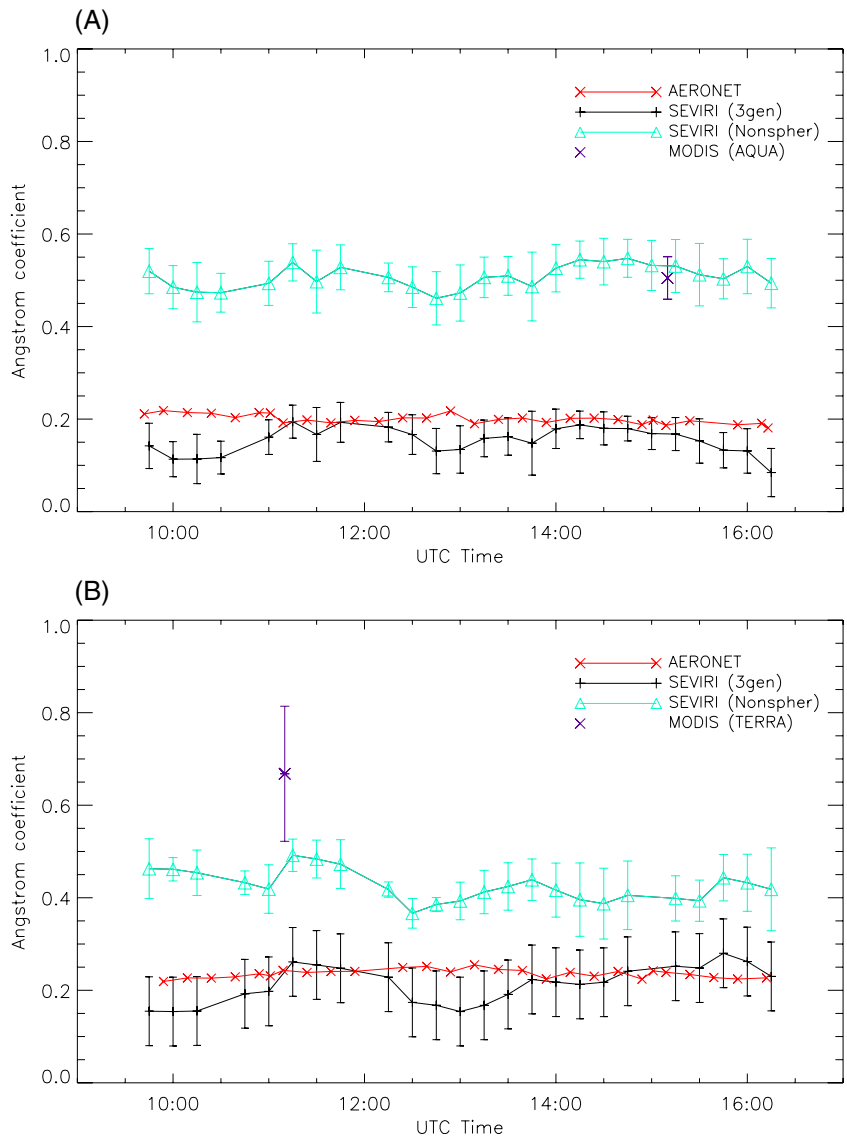

Fig. 14. Time-series of the Ångström Exponent derived from AERONET observations and retrieved from SEVIRI using the 3gen and Nonspher LUTs over Dakar on (A) 12th October, 2004; (B) 13th October, 2004. Corresponding MODIS values are also indicated when available. Vertical bars indicate the one-standard deviation spread in the SEVIRI derived AEs due to the spatial variability in the retrieved optical depths.

previous section is also shown. For the one time point available the MODIS AE value is ~0.1 larger than those obtained from either the AERONET measurements or the SEVIRI retrievals.

3.2. Case study 2: 12–13th October, 2004

To further investigate the performance of the retrieval algorithm the results from a second case study are presented in the following two sub-sections. On this occasion the dust event was much more localised, centred off the west coast of Senegal, persisting for approximately five days from 10–14 October, 2004, and peaking in intensity on the 12th. As before, analyses were performed with all four models, but in what follows, only 3gen and Nonspher results are discussed. The Opac and Des retrievals continue to show large disagreements with both MODIS and AERONET data, and were omitted from further discussion which concentrates on the two best performing candidate models.

3.2.1. Aerosol optical depth

The top row of Fig. 11 shows AOD fields derived from one 5-minute *Aqua*/MODIS granule taken from 15:10–15:15 UTC on 12th October 2004. Corresponding AODs retrieved from observations in the three SEVIRI bands during the 15:15 UTC time-slot (scaled to MODIS wavelengths of 0.644, 0.855 and 1.632 μm) are presented in the middle and bottom rows of Fig. 11. The fields shown in the middle row were obtained using the 3gen aerosol model, while those in the bottom row were retrieved using the Nonspher aerosol model. In general all three retrievals show a similar spatial pattern, although the more granular structure of the SEVIRI derived AODs towards the west of the image (for example in the vicinity of the Capo Verde islands) suggests that some residual cloud may not have been

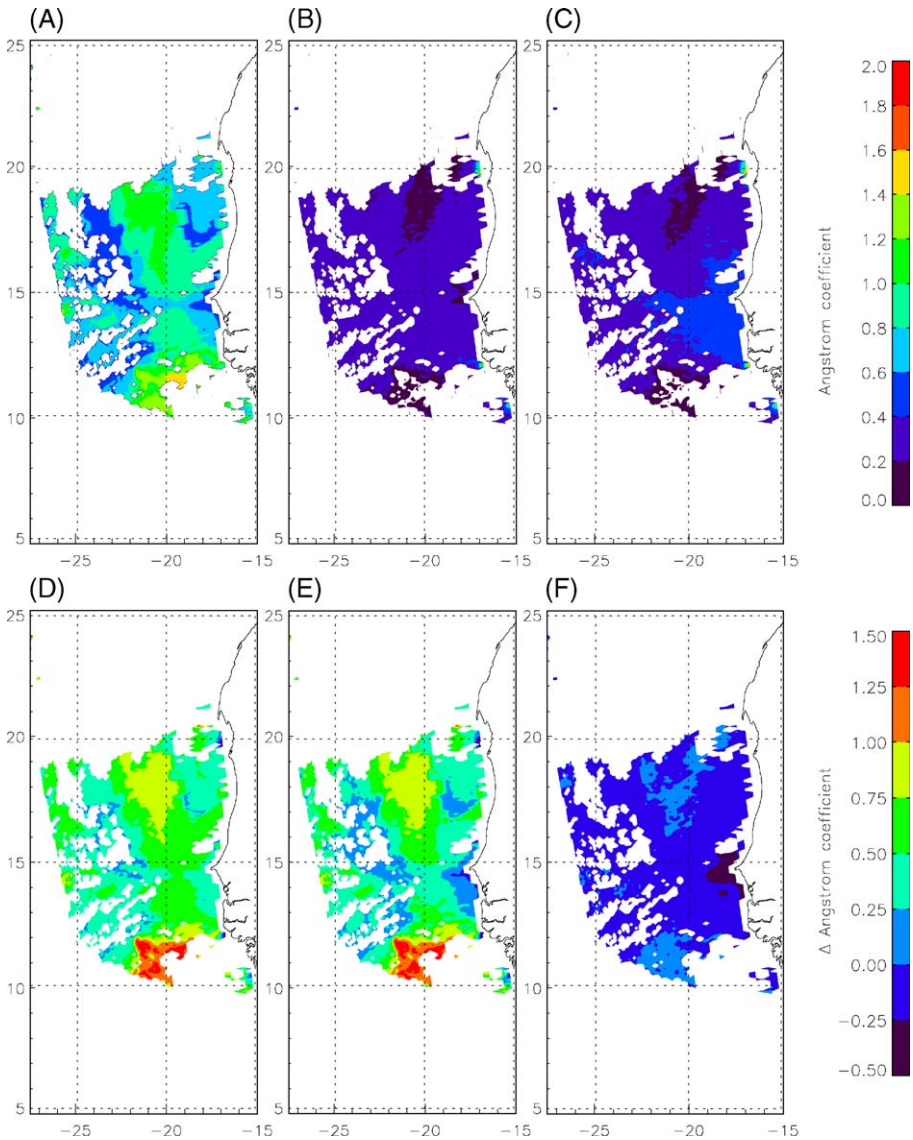

Fig. 15. (A) Ångström Exponent calculated from *Aqua*/MODIS retrievals shown in Fig. 11(A,B); (B) As (A) but using SEVIRI 3gen retrievals shown in Fig. 11(D,E); (C) As (A) but using SEVIRI Nonspher retrievals shown in Fig. 11(G,H); (D) MODIS–SEVIRI 3gen AE differences; (E) As (D) but for MODIS–SEVIRI Nonspher; (F) As (D) but for SEVIRI 3gen–SEVIRI Nonspher.

detected in the SEVIRI data by the MPEF algorithm. Both sets of SEVIRI AODs tend to be slightly higher than their MODIS counterparts, a pattern of behaviour reflected in Fig. 12, which shows density plots of the MODIS versus SEVIRI retrievals over the region for the given time-slot for each aerosol model. Table 5 summarises the comparisons by providing details of the mean channel differences and their standard deviation and range across the image. Results for the corresponding comparison of SEVIRI at 12:15 UTC versus *Terra*/MODIS observations from 12:05–12:10 UTC are also included. There is a good consistency with the "SEVIRI versus *Aqua*/MODIS" comparisons three hours later.

Although both the 3gen and Nonspher retrievals compare well with MODIS (the Nonspher retrievals being somewhat closer to MODIS in both mean bias and root-mean-squared deviation), the ultimate test is through comparison with ground-based sun-photometer data. Given the location of the maximum dust loading, the ability of the aerosol models to capture the temporal evolution of the storm was further tested through a comparison with AERONET observations made at the Dakar station (14.38°N, 16.95°W). Note that these AERONET data comprise level 1.5 data — that is they are automatically cloud cleared but may not have had a final calibration applied. However, the effect of calibration errors of a few percent will be negligible for the large optical depths observed over the period under consideration.

Fig. 13(A) and (B) show the ground based measurements and retrievals (adjusted to 0.67 μm) as a function of time for the 12th and 13th October respectively. Again, given that the SEVIRI based retrievals are obtained over ocean only, the values shown comprise an average from the three ocean pixels located within 14.25–14.5°N and 16.95–17.1°W. On both days the temporal evolution measured by the ground-based and SEVIRI 3gen observations agrees very well, with the only noticeable discrepancy seen during

the mid-morning on the 13th. However, similar to the results seen over Capo Verde in Fig. 11(A), the 3gen retrievals consistently underestimate the AERONET observations. On the 12th the daily mean AOD given by the 3gen SEVIRI retrievals is 1.67 compared to an AERONET value of 1.99. On the 13th, these quantities are 1.01 and 1.17 on the 13th, again a 15–20% underestimate in the 3gen retrievals.

Turning to the Nonspher SEVIRI retrievals, consistent with the March results, the broad pattern of behaviour of AOD with time is fairly similar to that obtained using the 3gen aerosol model. Nevertheless, there are obvious consistent differences between the two models on both days. Between approximately 11:00 and 12:30 UTC the Nonspher values are substantially lower than their 3gen counterparts, while the increase in AOD seen between 12:45 and 16:00 UTC is steeper in the Nonspher case, particularly on the 12th. The behaviour of χ with time (not shown) is very similar to that seen during the March event (Fig. 9(A)). Hence the late morning dip in AOD is due to the enhanced dependence of the Nonspher phase function on χ when $\chi > 165°$ compared to the 3gen model (Fig. 3(C)).

To complete the comparison the available MODIS retrievals are superimposed on each time-series at 15:10 UTC on the 12th (from *Aqua*) and at 11:10 UTC on the 13th (from *Terra*). The values shown are an average of those points within 0.5° of the Dakar site. On both days the spatial gradient of the retrievals over this region is relatively large. This results in AOD standard deviations of 0.74 (12th) and 0.22 (13th), indicating that the range of the MODIS retrievals easily encompasses both the AERONET and SEVIRI values.

3.2.2. Ångström exponent (AE)

Consistent with the results from case study 1 the AEs calculated using the SEVIRI 3gen retrievals for both the 12th and 13th October tend to be smaller than those derived from the AERONET observations (Fig. 14(A) and (B)). Accounting for the spread in the SEVIRI AE values due to the spatial variability in the retrieved optical depths generally results in overlap between the two time-series. Interestingly, the point MODIS values are substantially higher than both the AERONET and 3gen SEVIRI AEs. However, AEs calculated using SEVIRI Nonspher retrievals are more consistent with the MODIS values. To investigate whether both patterns of behaviour are spatially coherent, Fig. 15(A) illustrates the MODIS AE, estimated by applying Eq. (12) to the two MODIS AODs shown in Fig. 11(A) and (B). Corresponding SEVIRI values at 15:15 UTC, derived from band 1 and 2 AODs obtained using the 3gen and Nonspher aerosol models are shown in Fig. 15(B) and (C) respectively. For both models, the "MODIS minus SEVIRI" differences shown in Fig. 15(D) and (E) are positive across virtually the entire region. The largest differences between the two sets of SEVIRI AEs are those seen just off Senegal (Fig. 15(F)), precisely the region highlighted by the AERONET comparisons.

4. Conclusions and future work

A retrieval scheme based on the NOAA/NESDIS single-channel operational algorithm used to derive aerosol optical depths and Ångström Exponents from the visible channels of the polar orbiting AVHRR instrument has been adapted in order to infer the same quantities from the reflectances observed in the 0.6, 0.8 and 1.6 μm channels on the SEVIRI instrument, flying on the geostationary Meteosat-8 satellite. While the scheme is capable of retrieving AOD and size information for all aerosol types, this study has focused on the quality of retrievals that might be expected in the presence of mineral dust.

A key aspect of the scheme is the ability of the simulated single-channel reflectance LUTs to accurately represent the aerosol characteristics. Clearly, the aerosol model used in the generation of the LUTs plays a crucial role in determining the quality of the retrievals, especially when aerosol loading is high. Four models, one generic, and three selected for their potential to represent 'average' dust aerosol in global retrievals, are considered in detail.

For both the dust events considered here the LUTs based on Mie-calculated aerosol optical properties using the dedicated OPAC and Shettle desert-like dust microphysical models do not capture the temporal behaviour of the AOD, principally due to the strong dependence of their Mie-calculated phase functions on scattering angle in the back-scatter region. The large increase in the phase function with scattering angle between 150° and 180° results in a substantial, and consistent underestimate of AOD when this viewing condition is met.

On the other hand, the mono-modal, non-absorbing, 3rd generation NESDIS AVHRR aerosol representation introduced by Ignatov and Stowe (2002) provides a much better match to complementary observations of the AOD and Ångström Exponent made during the two dust events studied. Snapshot comparisons made with retrievals from the MODIS instrument show a mean agreement in AOD of ~0.1 at 0.644 μm, although the spatially resolved differences can be substantial (>|2.0|) in optically thick regions (AOD>4.0). Analysis of the time evolution of the AOD over the Capo Verde and Dakar sites indicates close agreement between the temporal behaviour of ground based AERONET observations and the SEVIRI retrievals obtained using this aerosol model. The absolute values of the ground based and SEVIRI derived AODs also show reasonable agreement although the satellite retrievals tend to be biased low relative to the AERONET measurements. The SEVIRI-derived Ångström Exponents also agree well with AERONET, given the spatial variability associated with the retrievals, whereas Ångström Exponents calculated from the available MODIS retrievals are consistently larger than both the SEVIRI and AERONET values.

The optical properties (extinction coefficients, single scattering albedos, and phase functions) for both the desert-like and the generic NESDIS aerosol models were derived under the assumption of particle sphericity. As a rule, the non-spherical phase functions are much flatter in the backscatter regime compared to the Mie calculation for large dust particles (e.g. Dubovik et al., 2002a,b; Mishchenko et al., 1995). Given this, the final model tested here was derived from average AERONET dust retrievals with the assumption that the particles were randomly orientated spheroids (Dubovik et al., 2002a,b). Compared to the spherical dust representations, the results

obtained using this non-spherical model are much more consistent with both the MODIS and AERONET observations, and with those obtained using the NESDIS aerosol model. The physical basis for the non-spherical model is also much stronger than that for the NESDIS aerosol model, which is essentially a match to an empirically derived phase function, with aerosol microphysics derived using Mie calculations to fit this empirical phase function. It thus may very well be that the NESDIS 3rd generation model comprises a fortuitous combination of non-representative aerosol microphysics with a not fully appropriate Mie calculation. As such, it clearly has room for improvement. However many more analyses with globally representative data are needed to come up with a well justified successor to the current empirical NESDIS model. To that end, the geostationary platforms provide a unique insight into the aerosol model improvement, which will also benefit aerosol retrievals from polar platforms. These analyses are currently underway, and their results will be reported elsewhere.

The assumption of sphericity may also have important consequences for the accuracy of mineral aerosol radiative perturbation estimates (Bellouin et al., 2004). In future work we plan to further assess the impact of the spherical particle assumption in the context of the SEVIRI observations, with a particular view to improving the radiative flux estimates available from GERB in the presence of mineral aerosol. In addition, by utilizing individual AERONET retrievals of size distribution and refractive indices over a larger sample of dust events we will be able to investigate how the application of a generic dust model may affect both the retrieval quality and the corresponding flux estimates.

Acknowledgements

Thanks to colleagues at RMIB for supplying the SEVIRI and GERB-like data, to NASA for providing access to the MODIS observations, and to Didier Tanré for his effort in establishing and maintaining the Capo Verde (Sal) and Dakar AERONET sites. Special thanks to Oleg Dubovik for providing the non-spherical aerosol model. Thanks also to two anonymous reviewers for their helpful suggestions for improving the manuscript. HEB is funded by the Natural Environment Research Council, UK under grant NER/I/S/2002/00698 and AI is funded under the NASA EOS/CERES (NASA contract L-90987C). The views, opinions, and findings contained in this report are those of the authors and should not be construed as an official NOAA or U.S. Government position, policy, or decision.

References

Bellouin, N., Boucher, O., Vesperini, M., & Tanré, D. (2004). Estimating the direct aerosol radiative perturbation: Impact of ocean surface representation and aerosol non-sphericity. *Quarterly Journal of the Royal Meteorological Society*, *130*, 2217−2232.

Brindley, H., & Russel, J. 2006. Improving GERB scene identification using SEVIRI: Infra-red dust detection strategy. Submitted for publication to *Remote Sensing of the Environment*.

Clerbaux, N., & Dewitte, S. (1999). RGP-SP: Spectral modelling. *RMIB technical report MSGRMIB-GE-TN-0005, RMIB* available from http://gerb.oma.be/

Dubovik, O., Holben, B., Eck, T., Smirnov, A., Kaufman, Y., King, M., et al. (2002a).Variability of absorption and optical properties of key aerosol types observed in worldwide locations. *Journal of the Atmospheric Sciences*, *59*, 590−608.

Dubovik, O., Holben, B., Lapyonok, T., Sinyuk, A., Mishchenko, M., Yang, P., et al. (2002b). Non-spherical aerosol retrieval method employing light scattering by spheroids. *Geophysical Research Letters*, *29*, 1415. doi:10.1029/2003GL018697

Gordon, H., & Morel, P. (1983). *Remote assessment of ocean color for interpretation of satellite visible imagery: A review: Springer Verlag. 114 pp.*

Govaerts, Y., & Clerici, M. (2004). MSG-1/SEVIRI solar channels calibration commissioning activity report. *EUM/MSG/TEN/04/0024, EUMETSAT* available from http://www.eumetsat.int/en/area2/publications/

Griggs, M. (1975). Measurements of atmospheric aerosol optical thickness over water using ERTS-1 data. *Journal of the Air Pollution Control Association*, *25*, 622−626.

Harries, J., Russell, J., Hanafin, J., Brindley, H., Futyan, J., Rufus, J., et al. (2005). The Geostationary Earth Radiation Budget (GERB) Project. *Bulletin of the American Meteorological Society*, *86*, 945−960.

Hess, M., Koepke, P., & Schult, I. (1998). Optical properties of aerosols and clouds: The software package OPAC. *Bulletin of the American Meteorological Society*, *79*, 831−844.

Holben, B. T., Eck, I., Slutsker, D., Tanré, J., Buis, A., Setzer, E., et al. (1998). AERONET — A federated instrument network and data archive for aerosol characterisation. *Remote Sensing of Environment*, *66*, 1−16.

Ignatov, A., Minnis, P., Loeb, N., Wielicki, B., Miller, W., Sun-Mack, S., et al. (2005). Two aerosol products over ocean on the Terra and Aqua CERES SSF datasets. *Journal of the Atmospheric Sciences*, *62*, 1008−1031.

Ignatov, A., & Stowe, L. (2000). The physical basis, premises, and self-consistency checks of aerosol retrievals from TRMM VIRS. *Journal of Applied Meteorology*, *39*, 2259−2277.

Ignatov, A., & Stowe, L. (2002). Aerosol retrievals from individual AVHRR channels. Part I: Retrieval algorithm and transition from Dave to 6S radiative transfer model. *Journal of the Atmospheric Sciences*, *59*, 313−334.

Ipe, A., Bertrand, C., Clerbaux, N., Dewitte, S., & Gonzalez, L. (2004). Validation and homogenization of cloud optical depth and cloud fraction retrievals for GERB/SEVIRI scene identification using Meteosat-7 data. *Atmospheric Research*, *72*, 17−37.

Jankowiak, I., & Tanré, D. (1991). Satellite climatology of Saharan dust outbreaks: Method and preliminary results. *Journal of Climate*, *5*, 646−656.

Kaufman, Y., Holben, B., Tanré, D., Slutsker, I., Smirnov, A., & Eck, T. (2000). Will aerosol measurements from Terra and Aqua polar orbiting satellites represent the daily aerosol abundance and properties? *Geophysical Research Letters*, *27*, 3861−3864.

Lutz, H. (1999). *Cloud processing for METEOSAT second generation. Technical Memorandum*, *vol. 4*. Darmstadt, Germany: EUMETSAT.

Mishchenko, M., Lacis, A., Carlson, B., & Travis, L. (1995). Non-sphericity of dust-like tropospheric aerosols: Implications for aerosol remote sensing and climate modelling. *Geophysical Research Letters*, *22*, 1077−1080.

Monahan, E., & Muircheartaigh, I. (1980). Optimal power-law description of oceanic whitecap coverage dependence on wind speed. *Journal of Physical Oceanography*, *10*, 2094−2099.

Moulin, C., Guillard, F., Dulac, F., & Lambert, C. (1997). Long-term daily monitoring of Saharan dust load over ocean using Meteosat ISCCP-B2 data 1. Methodology and preliminary results for 1983–1994 in the Mediterranean. *Geophysical Research letters*, *102*, 16947−16958.

Neckel, H., & Labs, D. (1984). The solar radiation between 3300-A and 12500-A. *Solar Physics*, *90*, 205−258.

Remer, L., Kaufman, Y., Tanré, D., Mattoo, S., Chu, D., Martins, J., et al. (2005). The MODIS aerosol algorithm, products, and validation. *Journal of the Atmospheric Sciences*, *62*, 947−973.

Schmetz, J., Pili, P., Tjemkes, S., Just, D., Kerkmann, J., Rota, S., et al. (2002). An introduction to Meteosat Second Generation (MSG). *Bulletin of the American Meteorological Society*, *83*, 977−992.

Shettle, E. (1984). Optical and radiative properties of a desert aerosol model. In G. Fiocco (Ed.), *Proceedings of the Symposium of Radiation in the Atmosphere* (pp. 74−77). Perugia, Italy.

Smirnov, A., Holben, B., Eck, T., Dubovik, O., & Slutsker, I. (2000). Cloud screening and quality control algorithms for the AERONET data. *Remote Sensing of Environment*, *73*, 337−349.

Tanré, D., Kaufman, Y., Herman, M., & Mattoo, S. (1997). Remote sensing of aerosol properties over oceans using the MODIS/EOS spectral radiances. *Journal of Geophysical Research*, *102*, 16971−16988.

Vermote, E., Tanré, D., Deuze, J. -L., Herman, M., & Morcrette, J. -J. (1997a). Second simulation of the satellite signal in the solar spectrum, 6S: An overview. *IEEE Transactions Geoscience Remote Sensing*, *35*, 675−686.

Vermote, E., Tanré, D., Deuze, J. -L., Herman, M., & Morcrette, J. -J. (1997b). *Second simulation of the satellite signal in the solar spectrum, (6S), 6S user guide version 2.* 218 pp. Available from ftp://loaser.univ-lille1.fr/6S/

Viollier, M., Tanre, D., & Deschamps, P. (1980). Algorithm for remote sensing of water color from space. *Boundary Layer Meteorology*, *18*, 247−267.

Wang, J., Liu, X., Christopher, S., Reid, J., Reid, E., & Maring, H. (2003). The effects of non-sphericity on geostationary satellite retrievals of dust aerosols. *Geophysical Research Letters*, *30*, 2293. doi:10.1029/2003GL018697

World Climate Program, WCP-55. (1983). Report of the expert meeting on aerosols and their climatic effects. In A. Deepak & H.E. Gerber (Eds.), Geneva: World Meteorological Organization. 83 pp.

World Climate Program, WCP-112. (1986). *A preliminary cloudless standard atmosphere for radiation computations.* Geneva: World Meteorological Organization, WMO/TD-N24. 83 pp.

Zhao, T., Laszlo, I., Dubovik, O., Holben, B., Sapper, J., Tanré, D., et al. (2003). A study of the effect of non-spherical dust particles on the AVHRR aerosol optical thickness retrievals. *Geophysical Research Letters*, *30*, 1317. doi:10.1029/2003GL018697